RESEARCH ARTICLE

ADVANCED
INTELLIGENT
SYSTEMS
Open Access

www.advintellsyst.com

Use of Superhydrophobic Surfaces for Performance Enhancement of Aerial–Aquatic Vehicles

Daniel Gortat, Alejandro Ortega Ancel, Andre Farinha, Raphael Zufferey, and Mirko Kovac*

Aerial–aquatic robotic vehicles show great potential in assisting in disaster response and environmental monitoring. However, to undertake these missions, they need to overcome the challenges of power requirements for takeoff and the difficulty of transitioning reliably between the air and water media. The use of superhydrophobic surfaces offers solutions to these challenges by reducing the wetted surface area of such robotic vehicles. In this article, a range of super-hydrophobic surfaces is analyzed for wettability and robustness performance to ascertain their benefits as a design feature for drag reduction in aerial–aquatic robotic vehicles. The silicon dioxide nanoparticle spray coating show the most superhydrophobicity measuring a static water contact angle of 174.8°. The coating's robustness tests yield a similar performance to that of laser-engraved brass with 200 μm groove separation, displaying a contact angle of 133.0° after ten finger strokes. The silicon dioxide nanoparticle spray is then used for drag reduction testing due to its ease of coating complex 3D geometries among the techniques explored in this study. The spray is applied to the hull of a sailing–flying robot, which resulted in the robot's drag reduction averaging 40% in the hydroplaning regime.

1. Introduction

The current field of micro-robotic systems has demonstrated the capability of operating effectively on land, air, and water. However, in applications where the robotic vehicles are required to transition between the media, such as air and water for environmental monitoring or underwater surveying, they prove to

D. Gortat, A. O. Ancel, A. Farinha, R. Zufferey, M. Kovac
Aerial Robotics Laboratory
Imperial College London
South Kensington Campus, London SW7 2AZ, UK
E-mail: m.kovac@imperial.ac.uk

M. Kovac
Materials and Technology Centre of Robotics
EMPA—Swiss Federal Laboratories for Materials Science and Technology
8600 Dübendorf, Switzerland

The ORCID identification number(s) for the author(s) of this article can be found under https://doi.org/10.1002/aisy.202100185.

experience tradeoffs in propulsion, structural design, and vehicle configuration.[1–3] Superhydrophobic surfaces show great potential in providing performance benefits for aerial–aquatic robots as a passive drag reduction technique. Such surfaces do not add complexity or significant additional mass to the vehicle nor do they need actuators to display the desired properties on the vehicle they are applied to. In addition, superhydrophobic surfaces can exhibit self-cleaning properties, preventing dirt or contaminants dissolved in water to adhere to the robot's surface, providing corrosion and fouling resistance.[4]

This paper examines the application of superhydrophobic surfaces in drag reduction, which small unmanned aerial–aquatic vehicles (UAAVs) can utilize to minimize their power consumption and improve their mission capabilities when transitioning between air and water.

Superhydrophobic surfaces are defined as surfaces with which, when laid flat, a drop of water forms an angle larger than 150°.[5] Superhydrophobicity is achieved by producing a surface topology, which enables gas to be trapped in surface voids preventing the liquid from penetrating. This is referred to as the Cassie–Baxter state.[6] The required surface topology must have roughness in the micrometer range or smaller, with surfaces consisting of nanometer scale structures typically achieving higher contact angles. These can also be combined, forming surfaces that have nanometer scale roughness on top of micrometer scale structures, with the purpose of minimizing the contact area of the water with the surface, known as the Lotus state.[7]

The use of superhydrophobic surfaces for drag reduction is a developing field that is recently gaining traction.[8] So far, the focus of the research in the field has been primarily on micro-channel flow and less research has been carried out on external hydrodynamics over 3D geometries. As such, questions remain about the fundamentals of drag reduction over these surfaces, especially in the turbulent regime.[8] For the laminar flow through a micro-channel up to 40% reduction in pressure drop was found when the walls were made superhydrophobic by etching a series of square wave patterns onto them.[8] Another channel flow study found no drag reduction for laminar flow but up to 50% drag reduction in the turbulent flow regime.[9] These experiments also showed a large reduction in drag with

**ADVANCED
SCIENCE NEWS**

www.advancedsciencenews.com

**ADVANCED
INTELLIGENT
SYSTEMS**
Open Access

www.advintellsyst.com

increasing Reynolds number for a particular geometry as well as with an increased feature size and spacing for a given Reynolds number.[9] Recently, similar results were found in numerical simulations of channel flow, where the drag reduction in turbulent flow was observed to be significantly greater than that for laminar flow.[10] Furthermore, the results agree with numerical simulations that also suggested that the modification of near-wall turbulent structures was a greater factor in turbulent drag reduction than effective slip on the air–water interface.[10,11] Moreover, the orientation of the surface features was shown to be important, since, when the surface grooves and ridges were aligned with the flow, drag reduction was achieved while an increase in drag was found when these run perpendicular to the flow.[10] However, drag reduction for turbulent flow over a hydrofoil coated with a nonstructured superhydrophobic surface has also been reported.[12]

Superhydrophobicity can also be used to design stimulus-responsive actuators that are able to respond to the external environment and convert external energy into dynamic movement. Recently, light-driven self-propelled actuators have been produced with the help of new materials, such as fluorinated acidified carbon nanotubes (F-ACNTs)/Fe3O4 nanoparticles.[13] Another study was able to develop a flexible superhydrophobic and photothermal paper based on ultralong hydroxyapatite nanowires for controllable light-driven self-propelled motion.[14] Both introduce a thin air layer between the coating and the water surface to reduce the fluid drag.

Robustness is another important performance metric to take into account for the choice of superhydrophobic surface for UAAV application. Superhydrophobic surfaces are prone to losing their properties through either damage to their delicate topology or contamination that alters their surface energy.

In this article, we fabricate a range of superhydrophobic surfaces, the performance of which is analyzed using the contact angle measurements and droplet bounce tests. Their robustness properties are compared before and after damage with finger stoking and the Stanley cutting knife. Finally, a drag reduction study is performed on a miniature polystyrene boat hull coated with a silicon dioxide nanoparticle spray to determine the skin friction reduction during its hydroplaning.

2. Experimental Section

The materials used in the study for the hydrophobic surface fabrication were CZ108 brass, a copolymer adhesive, and polytetrafluoroethylene sheets.

For the drag reduction study, the boat hulls, 320 mm length, 58 mm width, 45 mm depth, were fabricated using vacuum formed high impact polystyrene. The afterbody sidewalls of the hulls were tapered in by 4°. The radius of the bow was 160 mm and the deadrise angle counted 10°. Additional information on the design of the hull could be found in ref. [15].

2.1. Characterization Methods

The contact angle on the different surfaces was measured using the sessile drop technique, using the Young–Laplace fitting method on a Kruss Drop Shape Analyzer DSA100. The droplet size chosen to make the measurements was 7 μm, according to the manufacturer's recommended size. Five measurements were performed for each sample, and a deviation of 0.1° was obtained.

The droplet bounce tests were performed with the 27-G droplet depositing needle tips coated with nanoparticle spray to lower the tips' surface energy. A 7 μL drop was dispensed room temperature at a height of 20 mm from the surface tested to provide the most consistent results.[16] Each test was recorded with a Fastec TS5 high-speed camera at 529 frames per second.

The method chosen to analyze robustness was measuring the droplet contact angle at the surfaces before and after damage. Manual handling was considered to be the most likely way to damage the surface of a robot (through the force of rubbing and skin oils which can modify the surface chemistry), followed by impact or scratching against other abrasive surfaces. Consequently, the contact angle for all surfaces was compared after being rubbed with an index finger 1, 3, and 10 times, with a force of ≈8 N. Additional tests involved scratching the surface of the laser-engraved surfaces with a Stanley knife as well as with 80 grit sandpaper, using weights to provide a pressure of exactly 10 N cm^{-2}.

The samples were imaged using a scanning electron microscope (SEM), Zeiss Auriga Cross Beam, and optical microscope, Zeiss AX10 with CCD camera AxioCam Erc 5c

The drag reduction study was done in a recirculating 9.0 m long, 0.6 m wide, and 0.6 m deep water flume. The hull was connected to a single-axis load cell with a 0.3 m long string, to allow free movement of the hull on the water surface without fixing its position and orientation. The load cell used was a Futek LB210 submersible S-beam cell, with a maximum load capacity of 1 N, chosen due to its high sensitivity. The load cell was positioned to achieve a string angle of ≈8° to simulate the effect of the tilted motor thrust, which would produce the equivalent force of the string tension during steady hydroplaning. A Nixon Streamflo series 403 flowmeter was used to measure the velocity of the water flow near the surface. The probe was placed sufficiently upstream to have a negligible effect on the flow around the hull. The schematic of the setup is shown in **Figure 1**. With a maximum speed of 1.53 m s^{-1}, the flume cannot replicate real operation conditions, thus, a decision was taken to use a real scale model. However, to capture the dragging to hydroplaning transition, the experiments were run at scaled-down mass. This means that even though drag results are not quantitatively relevant for real operating conditions, the lift force can be directly scaled, giving a reliable prediction of the speed at which hydroplaning transition occurs.

3. Sample Fabrication

Superhydrophobic surfaces were manufactured using three methods: silicon dioxide spray coating, polytetrafluoroethylene (PTFE) sanding, and metal laser engraving.

3.1. Silicon Dioxide Spray Coating

This manufacturing method requires an initial deposition of an adhesive substrate, onto which a layer of silicon dioxide particles with a diameter in the range of a few tens of nanometers is
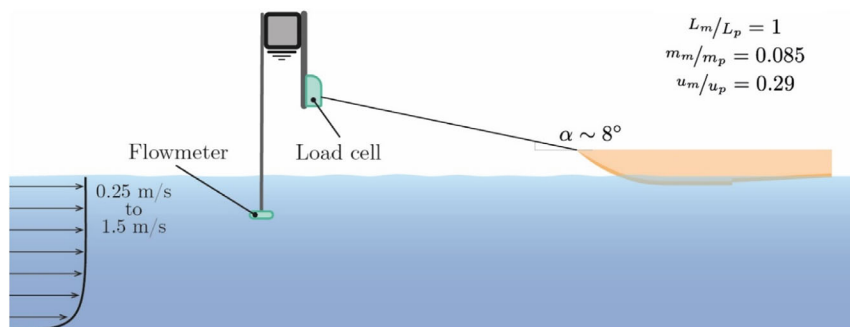
$$L_m/L_p = 1$$
$$m_m/m_p = 0.085$$
$$u_m/u_p = 0.29$$

$\alpha \sim 8°$

Flowmeter   Load cell

0.25 m/s to 1.5 m/s

Figure 1. Schematic of the drag reduction study experimental setup. The experiments were run at scaled down mass and speed.

embedded. By repeatedly applying the sprays, binding is ensured, creating clusters of particles, which form a hierarchical surface structure. This enhanced the roughness of the surface to improve the maintenance of the Cassie–Baxter state. **Figure 2** shows the SEM images taken at 14 000, 24 000, and 127 000 times magnification. The hierarchical nature of particle clusters can be seen in these images.

3.2. Sanded Polytetrafluoroethylene

PTFE was sanded with 240-grit paper in random and unidirectional manner. The unidirectional sanding produced filaments of PTFE with a diameter similar to that of the sandpaper grit size and length of 1–10 mm (**Figure 3**).

3.3. Laser Engraving

The laser system used to manufacture superhydrophobic surfaces on brass was pulsed A-series micromachining platform from Oxford Lasers, wavelength of 355 nm. The beam width of the laser at its focus was 8 μm. The laser frequency was set to 100 kHz for all sample manufacture in this study. The treatment was carried out at the atmospheric pressure in ambient air.

To lower the surface energy of the laser-engraved samples, a chemical treatment was performed using 1,1,2,2 H–perfluorooctyltriethoxysilane 98% from Sigma-Aldrich. The samples were treated in the following steps: 1) dilution of perfluorooctyltriethoxysilane in hexane (5% w/w); 2) inclination of the surfaces 80° to the vertical, to allow the liquid solution to flow down the surface; 3) coating of the surface with the solution using a

21-gauge syringe; and 4) drying of the surface in the fume hood for 20 min.

A range of 10 by 10 mm square samples of different patterns was prepared. Following parameters were chosen: 50 kHz repetition rate, 80 mm s^{-1} scanning speed, laser power of 12.4 W, and a pulse energy of 248.6 μJ.

The laser parameters were chosen to ensure a generation of the grooves in a single laser pass. Due to this relatively large laser power molten debris attached to the top of the groove walls, creating additional ridges (**Figure 4**). These ridges act as additional solid structure, which prevents the water from making contact with the surface.

Four different spacings between the micro-grooves were chosen: 20, 50, 100, and 200 μm. The samples were then treated and coated with 1,1,2,2 H–perfluorooctyltriethoxysilane to lower the surface energy. **Figure 5** shows the square pattern at the largest beam spacings.

4. Sample Characterization

A measurement of a flat brass surface coated with 1,1,2,2 H–perfluorooctyltriethoxysilane (PFOTES) was carried out as a baseline for comparison with the microstructured surfaces. The results are recorded in **Figure 6**.

The hierarchical structure created with the nanoparticle spray was found to be the most superhydrophobic with a contact angle of 174.8°. The results for the different laser-engraved patterns on brass treated with 1,1,2,2 H–perfluorooctyltriethoxysilane show that the contact angle varied very little for the different patterns, with all measurements being between 171.8° and 172.4°. This is
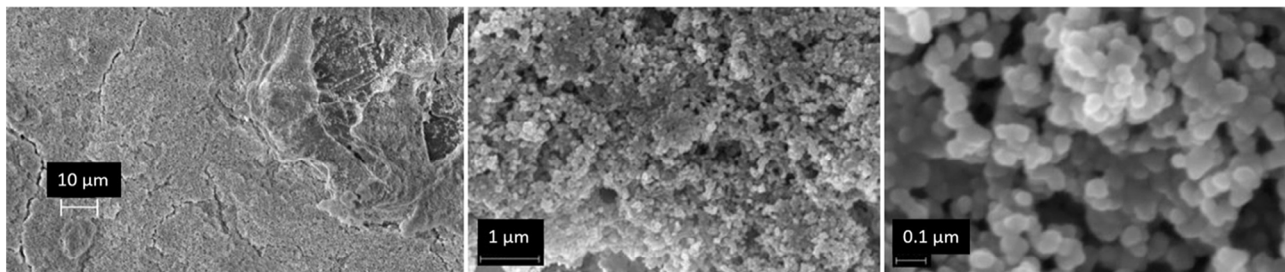

Figure 2. Scanning electron microscope (SEM) image of nanoparticle spray-coated surface at a magnification of 1,400x (left), 24,000× (center), and 127,000× (right).

**ADVANCED
SCIENCE NEWS**
www.advancedsciencenews.com

**ADVANCED
INTELLIGENT
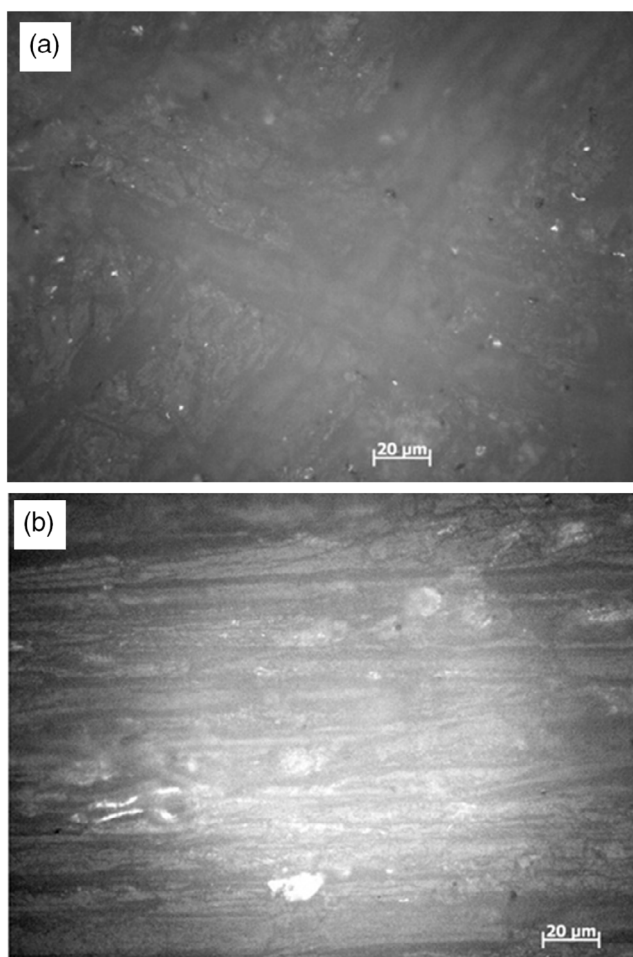SYSTEMS**
Open Access
www.advintellsyst.com

Figure 3. Optical microscope image of sanded polytetrafluoroethylene (PTFE). a) Random sanding pattern, b) directionally sanded pattern.

Figure 4. SEM image of brass engraved with a laser-beam spacing of 50 μm, at 12.4 W and 80 mm s^{-1} scanning speed, 1,900x magnification (15 kV SEM beam voltage).

attributed to the fluorite treatment of the samples, since other work has shown that different spacing and even different groove depths affect contact angle.[17,18]

Bounce tests were carried out on each of the different patterns laser engraved on brass, as well as PTFE, sanded PTFE, and plain brass, since the energy recovered by water droplets bouncing on a surface has shown to provide an indication of the hydrophobicity of a surface.[16] As expected, due to the lower contact angle, 8 bounces were recorded for the sanded PTFE, while no bounces were observed for the unmodified PTFE or unmodified brass. **Figure 7** shows the 28 s recording of the droplet bounces on laser-engraved brass, sanded PTFE, and unmodified brass. **Table 1** shows the number of bounces for each of the patterns on the laser-engraved brass. Similarly to the results from the contact angle measurements in Figure 6, there are no significant differences in bounces between the different laser-engraved patterns.

4.1. Chemical Etching

Another method for manufacturing superhydrophobic surfaces is chemical etching. This method was employed on the preparation of aluminum samples, a material commonly used in the aerospace sector. A bath of sulfuric acid at 40% v/v and a 3 A current were applied for 3 h, creating micro-pits of the order of 10 μm. The samples were then rinsed with deionized water and dipped in a 1% w/w solution of Trichloro(1,1,2,2 H– perfluorooctyl)silane in hexane for another 2 h. Finally, the samples were dried in an oven at 100 °C for 1 h.

The contact angle measured for this surface was 163.4°, which makes chemical etching an interesting method for fabrication of complex 3D-shaped superhydrophobic components. Unfortunately, most such components in unmanned aerial vechicle (UAV) systems tend to be fabricated out of polymeric materials, which require more complex fabrication methods, such as plasma etching. Spray coating (Section 3.1) is thus a more accessible method that can be applied to such surfaces.

5. Robustness Characterization

The robustness tests show that all of the laser-engraved patterns and the nanoparticle spray maintain high performance after a single-finger stroke, maintaining a contact angle within 1.0% of the non-damaged surface on average (**Figure 8**).

In contrast, the sanded PTFE lost its superhydrophobicity after just a single stroke, decreasing its contact angle by 7.6°, which could be due to its microstructure being less mechanically robust. The average decrease in contact angle for the laser-engraved surfaces after three strokes is shown to be 15.0° with similar performance for the different patterns. The nanoparticle spray and sanded PTFE, however, lost 19.7° and 19.9°, respectively. Much larger differences arose between the patterns after ten strokes, with the laser-engraved surfaces with laser-beam separations of 100 and 200 μm as well as the nanoparticle spray losing superhydrophobicity. A clear pattern for the laser-engraved surfaces emerges. The closer together the laser grooves, the better the performance. This proves that higher groove density results in improved robustness performance, with the 20 μm square pattern performing best at 153.6° contact angle, compared to 133.2° for the 200 μm line pattern. The nanoparticle spray performed similarly to the 200 μm line pattern after
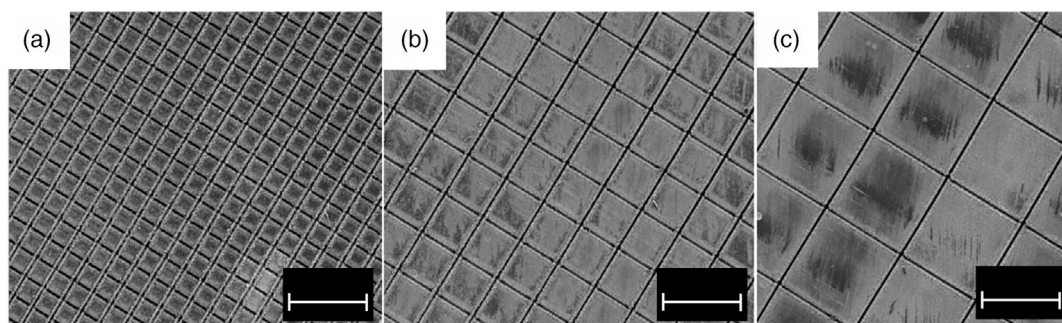
**ADVANCED
SCIENCE NEWS**

www.advancedsciencenews.com

**ADVANCED
INTELLIGENT
SYSTEMS**
Open Access

www.advintellsyst.com

Figure 5. SEM images of brass engraved with a laser-beam spacings of a) 50 µm, b) 100 µm, c) 200 µm, 100x magnification (15 kV SEM-beam voltage).
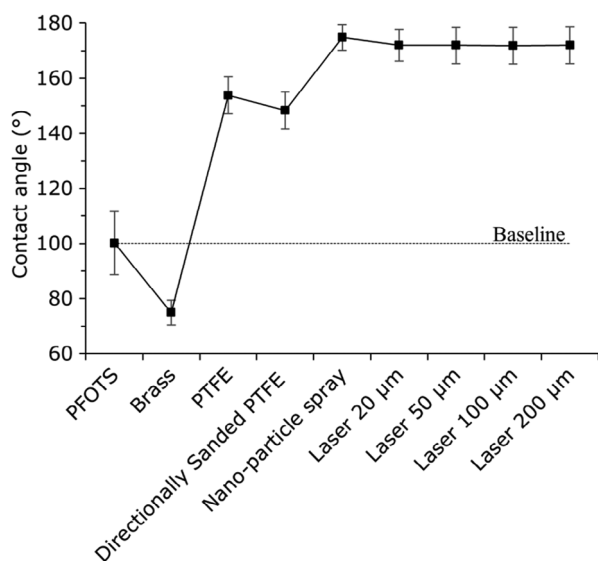

Figure 6. Contact angle measurements for nanoparticle spray, 1 H,1 H,2 H,2 H–perfluorooctyltriethoxysilane-treated laser-engraved brass, untreated brass, sanded PTFE, and laser-treated engraved brass.
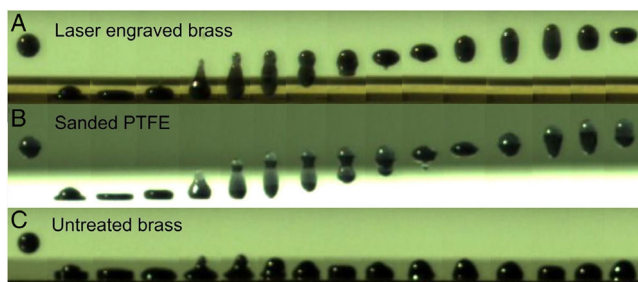

Figure 7. The 28 ms sequence for a 7 µL droplet dropped from 20 mm height on A) superhydrophobic brass, B) sanded PTFE, and C) untreated brass.

Table 1. Number of bounces of a 7 µL droplet of water dropped from a 20 mm height on laser-engraved brass.

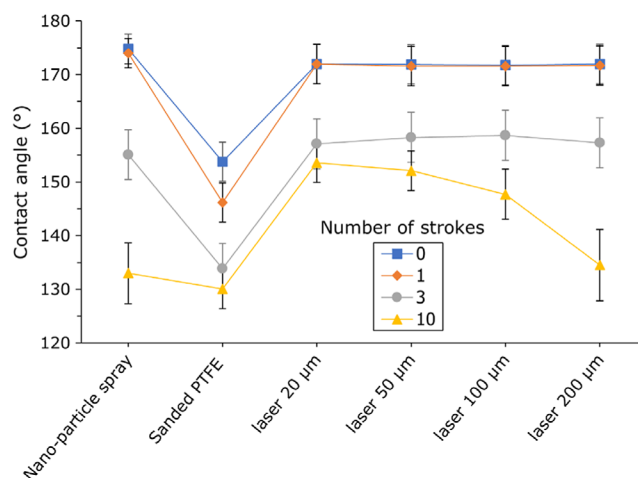| Laser-beam spacing [µm]	20	50	100	200
Number of bounces	10	10	11	11

Figure 8. Contact-angle measurements for nanoparticle spray, randomly sanded PTFE and laser-treated engraved brass following damage by an increasing number of finger stokes.

10 strokes, displaying a contact angle of 133.0° while the sanded PTFE was measured to be 130.1°.

The measurements after damage with sandpaper are comparable to those damaged with the finger, within ≈1.6° contact angle for all measurements. This suggests that the potential contamination by the skin oil on fingers is not a dominant factor in the contact angle decrease for these tests. However, the removal of the functionalized top layer of material, with a lower surface energy, might also be a contributing factor for both damage mechanisms. Damaging the samples with a Stanley knife had a less pronounced effect on the contact angle. Even the most heavily damaged surface remained superhydrophobic at a 153.1° contact angle (**Figure 9**). The cuts damage the surface by altering the geometry of the microstructure, as well as also removing the functionalized top layer of the surface. However, the knife cuts are localized and do not affect the entire surface, as is the case for the other two mechanisms. This could explain why the surfaces are more resistant to scratching by knife cuts than to different abrasion mechanisms.

The superior robustness performance of the laser-engraved surfaces could be explained by the strength of the metal oxide ridges compared to that of the adhesive, binding the nanoparticles together and the PTFE ridges. The improved robustness
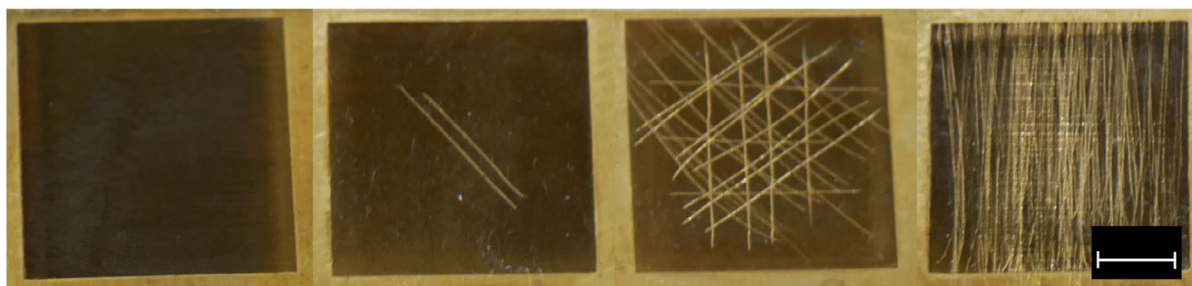
**ADVANCED
SCIENCE NEWS**

www.advancedsciencenews.com

**ADVANCED
INTELLIGENT
SYSTEMS**
Open Access

www.advintellsyst.com

Figure 9. Laser-engraved surfaces displaying damage by a variety of Stanley knife cuts.

with increasing groove density for the laser-engraved surfaces could be due to their greater number of ridges raising the probability that some ridges would remain undamaged.

As such, the laser-engraved surfaces can have tailored robustness properties as well as superhydrophobicity, compared to other samples tested here, limited only by the manufacturing capabilities of the laser system. Thus, laser-engraving metal is the favorite for manufacture of robust superhydrophobic surfaces for drag reduction for UAAVs.

In the current study, the laser system was not able to perform 3D structuring of the surface of the UAAV's hull in Section 2 to analyze the effects of superhydrophobicity in the Kruss Kruss drag regime during horizontal takeoff at the water surface. Therefore, the authors opted for a silicon dioxide nanoparticle spray coating, which displayed the next most robust properties to that of the laser-engraved surfaces as well being the most superhydrophobic in the study.

6. Skin Friction Drag Reduction Study

Figure 10 illustrates the locomotion regimes a UAAV experiences during a horizontal takeoff.[15] First, the tests were performed in the displacement regime, relevant to low-speed operation, such as sailing and the beginning of the UAAV's takeoff run. Then, the performance during hydroplaning was studied, which is relevant to the last moments of takeoff, during which the UAAV accelerates to takeoff speed. Measurements were taken at water flow velocities of 0–1.53 m s^{-1}. The results are expressed as the ratio of inertial and gravitational forces (Froude number).

Experiments were run on the unloaded hulls, which corresponds to a beam-loading coefficient of 0.134. **Figure 11** shows the nondimensional values of drag over speed for these experiments, and Froude number and drag coefficient values were obtained using the geometrical quantities shown in **Table 2**, where area and length references were taken relative to the hull's wetted line in static conditions. The results show that superhydrophobicity has a negligible effect on drag at low beam loadings in the lower displacement regime, Fr < 0.3 or U < 0.7 m s^{-1}. In contrast, superhydrophobicity was observed to have a dramatic effect on drag during planning and around the transition region (Fr ≈ 0.5, U ≈ 0.7 m s^{-1}), the "hump," shown in Figure 10, exhibiting a smooth change between the displacement and hydroplaning regimes. The drag reduction was measured to be an average of 40% lower, with the highest reduction of 52% at the "hump." The effect of superhydrophobicity becomes
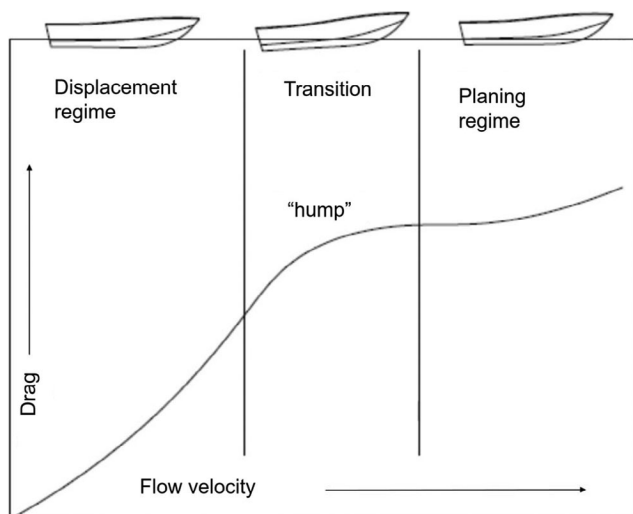

Figure 10. Diagram showing the different flow regimes for the hulls, highlighting the "hump" region during the transition between displacement and planning, when the rate of drag increase with flow speed is significantly diminished.
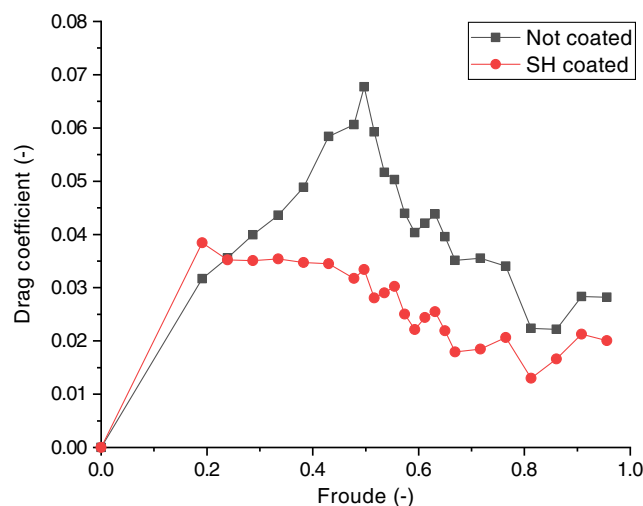

Figure 11. Drag coefficient versus Froude number for the hull designs, not coated, and the superhydrophobic hull, super hydrophobic (SH) coated, including the hydroplaning regime.

2100185 (6 of 8)

Table 2. Geometrical quantities and physical properties used to calculate the drag coefficients and Froude numbers.

$C_D = \frac{2F_D}{\rho u^2 A}$	$A = 0.003176 \text{ m}^2$	$\rho = 997 \text{ kg m}^{-3}$
$Fr = \frac{u}{\sqrt{gL}}$	$L = 0.255 \text{ m}$	$g = 9.81 \text{ m s}^{-2}$

less pronounced as the hulls enter the higher drag regime, with a drag reduction of 36% up to the maximum velocity tested.

The drag increases gradually throughout the transition regime, in a more linear manner, as the wetted surface area of the hull decreases with increase in speed. This phenomenon can be observed in **Figure 12**. The wetted area reaches a minimum at a flow speed of 1.28 m s^{-1}, Fr ≈ 0.8, where the drag reaches a local minimum. As the flow speed increases further, the hydrodynamic drag increases rapidly again.

The effects of superhydrophobicity on drag can be explained in part by the evolution of the wetted surface on the superhydrophobic hull. The wetted surface was observed to start shrinking at a lower speed than for the non-coated hull. The wetted surface area then remained smaller for the superhydrophobic surface during planning, with a smaller difference in area observed at the highest speeds tested.

It is well known that drag reduction with surface microstructure topology is not a straightforward process, requiring good knowledge of the flow field, boundary layer, and flow separation. In contrast, these results demonstrate that a simple surface preparation method can achieve considerable drag reductions in locomotion regimes where liquid–gas interfaces play a central role. Interestingly, this type of surface treatment produces higher drag at lower speeds, due to the spurious effect of increased surface roughness. In contrast, a considerable performance increase is seen in the region where Fr = 0.5. This region corresponds to maximum wave drag, when the hull displacement wave has a wavelength equal to 1.5 times the hull length. This positions the lowest point of the wave at 75% of the hull, near where the step is located, facilitating the entrance of air to the afterbody bubble, and reducing skin-friction drag. It is then no surprise that a surface with lower surface energy will further improve this drag reduction mechanism primarily around the hump region.
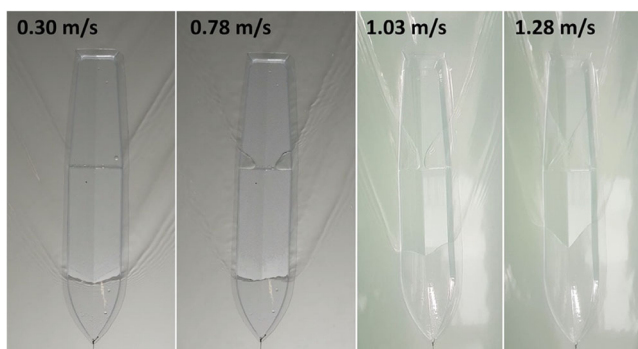
This improvement has a positive impact on the takeoff of aerial–aquatic hybrid UAVs, not only by decreasing the maximum engine power required due to the lower drag in planning, but also by reducing the amount of dynamic loading on the hull by flattening the drag curve around Fr = 0.5. For context, we can expect the 36% reduction in drag at higher speeds to cause up to 36% reduction in the necessary motor power, leading to considerable weight saving (brushless motors for micro aerial vehicle (MAV) scale currently stand at 0.5 W g^{-1}). While these improvements are shown here only in the hydroplaning regime, one can also expect performance improvements on the impulsive takeoff of aerial vehicles, where the reduction in wetted surface area reduces the airborne mass of the vehicle. This leads, in a best-case scenario, to a linear increase of the takeoff height or final takeoff speed.

7. Conclusion

The superhydrophobic surface analysis presented in this work can contribute to further development of aerial–aquatic robotics by providing a powerful method to enhance the performance of these vehicles. The potential performance enhancements focus on three main areas; reduction of hydrodynamic drag, shedding of water on the water-to-air transition to reduce airborne weight, and superhydrophobic surface robustness.

The manufacturing methods explored provide a wide range of options with a plethora of different characteristics to test their potential benefits for UAAVs. In summary, the results show that surperhydrophobicity can considerably reduce the wetted area in hydroplaning regime, resulting in an average drag reduction of 40%. Furthermore, the same effect is observed around the transition "hump" region, which can considerably reduce the power required for UAAVs. As well as that, depending on the material used for construction of the UAAV, the robustness performance can be increased by increasing the density of surface nanostructures, as demonstrated by the 20 μm square pattern performing best after 10 finger strokes at 153.6° contact angle, compared to 133.0° for the 200 μm line pattern on the laser-engraved brass surfaces and silicon dioxide nanoparticle spray, as long as the Cassie–Baxter state is maintained over most of the surface.

Conflict of Interest

The authors declare no conflict of interest.

Figure 12. Evolution of the wetted area as the flow speed is increased. A bubble of air behind the step separating the forebody and afterbody of the hull can be seen forming and growing as the hull transitions into hydroplaning.

Data Availability Statement

Data available in article supplementary material.

**ADVANCED
SCIENCE NEWS**

www.advancedsciencenews.com

**ADVANCED
INTELLIGENT
SYSTEMS**

www.advintellsyst.com

[1] V. M. Ortega-Jiménez, S. Álvarez-Borrego, S. Arriaga-Ramírez, M. Renner, and E. S. Bridge, *J Ornithol*, **2010**, *151*, 169.

[2] R. J. D. Siddall, *Aerial Aquatic Locomotion with Miniature Robots*, **2017**, Doctoral, Imperial College, London, https://doi.org/10.25560/68277.

[3] K. Nagatani, S. Kiribayashi, Y. Okada, K. Otake, K. Yoshida, S. Tadokoro, T. Nishimura, T. Yoshida, E. Koyangi, M. Fukushima, S. Kawatsuma, *J. Field Robot* **2013**, *30*, 44.

[4] T. Sun, L. Feng, X. Gao, L. Jiang, *Acc. Chem. Res.* **2005**, *38*, 644.

[5] S. Wang, L. Jiang, *Adv. Mater.* **2007**, *19*, 3423.

[6] A. B. D. Cassie, S. Baxter, *Trans. Faraday Soc.,* **1944**, *40*, 546.

[7] D. Murakami, H. Jinnai, A. Takahara, *Langmuir* **2014**, *30*, 2061.

[8] J. P. Rothstein, *Annu. Rev. Fluid Mech.* **2010**, *42*, 89.

[9] R. J. Daniello, N. E. Waterhouse, J. P. Rothstein, *Phys. Fluids* **2009**, *21*, 085103.

[10] H. Park, H. Park, J. Kim, *Phys. Fluids* **2013**, *25*, 110815.

[11] T. Min, J. Kim, *Phys. Fluids* **2004**, *16*, L55.

[12] S. Gogte, P. Vorobieff, R. Truesdell, A. Mammoli, *Phys. Fluids* **2005**, *17*, 051701.

[13] H. Wu, J. Luo, X. Huang, L. Wang, Z. Guo, J. Liang, S. Zhang, H. Xue, J. Gao, *J. Colloid Interface Sci.* **2021**, *603*, 282.

[14] R.-L. Yang, Y.-J. Zhu, F.-F. Chen, D.-D. Qin, Z.-C. Xiong, *ACS Sustain. Chem. Eng.* **2019**, *7*, 13226.

[15] R. Zufferey, A. O. Ancel, C. Raposo, S. F. Armanini, A. Farinha, R. Siddall, I. Berasaluce, H. Zhu, M. Kovac, *IEEE Robot. Autom. Lett.* **2019**, *4*, 2894.

[16] C.-V. Ngo, D.-M. Chun, *Appl. Surf. Sci.* **2017**, *409*, 232.

[17] C. R. Crick, I. P. Parkin, *Chem. Commun.* **2011**, *47*, 12059.

[18] D. V. Ta, A. Dunn, T. J. Wasley, R. W. Kay, J. Stringer, P. J. Smith, Colm Connaughton, J. D. Shephard, *Appl. Surf. Sci.* **2015**, *357*, 248.